# Dynamical correlation enhanced orbital magnetization in $VI_3$

Zhimou Zhou,[1] Shishir Kumar Pandey,[1] and Ji Feng[1,2,*]
[1]*International Center for Quantum Materials, School of Physics, Peking University, Beijing 100871, China*
[2]*Collaborative Innovation Center of Quantum Matter, Beijing 100871, China*

(Received 6 September 2020; revised 10 December 2020; accepted 11 January 2021; published 22 January 2021)

The effect of electronic correlations on the orbital magnetization in real materials has not been explored beyond a static mean-field level. Based on the dynamical mean-field theory, the effect of electronic correlations on the orbital magnetization in layered ferromagnet $VI_3$ has been studied. A comparison drawn with the results obtained from density-functional theory calculations robustly establishes the crucial role of dynamical correlations in this case. In contrast to the density-functional theory that leads to negligible orbital magnetization in $VI_3$, in dynamical mean-field approach the orbital magnetization is greatly enhanced. Further analysis shows that this enhancement is mainly due to the enhanced local circulations of electrons, which can be attributed to a better description of the localization behavior of correlated electrons in $VI_3$. The conclusion drawn in our paper could be applicable to a wide range of layered materials in this class.

DOI: 10.1103/PhysRevB.103.035137

## I. INTRODUCTION

Although in most of the materials electronic spin magnetization dominates their magnetic behaviors, in a few unusual magnetic materials orbital magnetization can be significant and even dominant [1–5]. Although its implications on the fascinating properties of a broader range of materials [6–10] is self-motivating, yet much of the attention has been paid to its spin counterpart. In contrast to atomic and molecular species where only local electronic circulation is possible, the orbital magnetization of a crystalline material comes from intracellular and intercellular circulations [11–16]. Often concomitant to magnetism is the most intricate issue of strong correlation effect, which usually incurs dramatic changes in the electronic structure. This begets a natural question whether and in what manner electronic correlation will affect the orbital magnetization in crystalline materials.

This interesting problem has been approached with various theoretical frameworks in previous studies, however, associated with them are their natural shortcomings. For example, in density-functional theory (DFT) with Hubbard $U$ correction, correlation effects were included only at the static mean-field level [17]. Studies on the related issue of exciton $g$-factor renormalization based on GW approximation [18–20], which although accounts for many-body effects at the perturbative level, only the simple formalism of orbital magnetic moments for noninteracting case was used. Although the modern theory of orbital magnetization has been generalized to interacting systems and applied to model systems [21–24], its applicability when dealing with real materials is yet to be established. Thus, a more generic approach to this problem would be to apply the formalism for the interacting case on a real material with proper treatment of electronic correlations beyond static mean-field level.

The stabilization of long-range magnetic order in layered magnetic materials, despite the celebrated Mermin-Wagner theorem [25], is due to the strong magnetic anisotropy through spin-orbit coupling, a direct consequence of the unquenched orbital moments of magnetic ions. A large number of layered materials contains transition-metal elements which are themselves magnetic in nature and exhibit strong electronic correlation. On top of that, the highly anisotropic nature of chemical bonding with strong in-plane and weaker interlayer cohesion, leads to reduction of electronic dimensionality. This, in turn, leads to reduced screening of the Coulomb interaction, hence, stronger electronic correlation. Thus, the question raised above becomes highly relevant to this class of materials. A unique advantage of these materials is that the individual layers can be removed and transferred to the desired substrate [26], yielding a quasi-two-dimensional monolayer.

Two-dimensional magnetism with long-range magnetic order has just been established in monolayer materials, such as $Cr_2Ge_2Te_6$ and $CrI_3$ [27–29]. In both of these Cr compounds, crystal-field splitted lower-lying $t_{2g}$ orbitals are fully filled with three electrons in the majority spin channel, leaving less room for the unquenched orbital moment. This observation makes a material with less than fully filled $t_{2g}$ orbitals all the more interesting. Recently reported $VI_3$, which is also suggested to be a layered van der Waals magnetic material, satisfies this precondition. It is found to display more complicated magnetic behavior compared to $CrI_3$ [30–33]. In particular, $VI_3$ is also suggested to be a Mott insulator and exhibits larger saturated magnetization along the $c$ axis than in the in-plane direction. More specifically, Tian *et al.* [30], reported a saturated magnetic moment of 2.47 $\mu_B$/V along the $c$ axis, slightly larger than the expected value from spin polarization, indicating an unquenched orbital magnetic moment. Past study on $YVO_3$ employing the Hartree-Fock ap-

*jfeng11@pku.edu.cn

 

proach also reported small but nonzero orbital magnetization [17]. Based on the above considerations, $VI_3$ seems to be a good platform to explore the effect of electronic correlation on orbital magnetization.

In this paper, we study the effect of dynamical correlations on the magnetic properties of $VI_3$. To this end, we use a combination of DFT + $U$ [34,35] and self-consistent DFT + dynamical mean-field theory [36] in our paper. Hereafter, we will refer to the latter method simply as DMFT. We find that compared to the static mean-field results from DFT + $U$ method, the dynamical correlations involved in the self-consistent DMFT framework enhance the orbital magnetization in $VI_3$ in both states, the high-temperature paramagnetic as well as the low-temperature ferromagnetic state. We find that dynamical correlation also stabilizes the orbital magnetization in the monolayer limit. This is a demonstration of the role of dynamical correlation in the orbital magnetization in real magnetic materials.

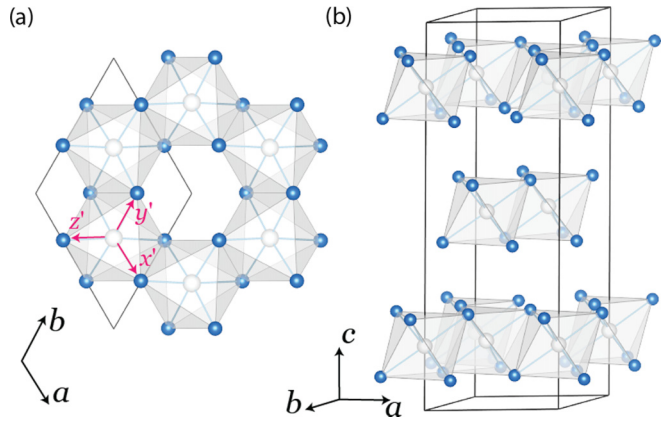


FIG. 1. Crystal structures of (a) monolayer, and (b) bulk $R\bar{3}$. The local Cartesian coordinates for the octahedral coordination $x' - y' - z'$ are indicated with red arrows.

## II. METHODS

For bulk calculations, the experimental lattice parameters are adopted [30,32]. For lattice relaxation of monolayer $VI_3$, we use the DFT as implemented in the Vienna *ab initio* simulation package [37,38]. The energy convergence criterion is $10^{-5}$ eV, and the interatomic force convergence for structure optimizations is 0.01 eV/Å. The DFT and DFT + $U$ electronic structure calculations are based on the full-potential linearized augmented plane-wave method as implemented in the WIEN2K package [34,35]. In DFT + $U$ calculations, the Hubbard $U$ correction is added through an effective $U_{\text{eff}} = U - J = 4$ eV [39]. The value of $U_{\text{eff}}$ is chosen by matching the computed gaps (0.67 and 0.64 eV for $R\bar{3}$ and $P\bar{3}1c$, respectively) to the experimentally observed optical band gap at room temperature (0.60 and 0.67 eV for $R\bar{3}$ [31] and $P\bar{3}1c$ [32], respectively). The local dynamical correlation of $d$ electrons is accounted for in the charge self-consistent DMFT calculations [36]. The spin-orbit coupling was included in both DFT + $U$ and DMFT calculations. In all DFT calculations, including the DFT steps in the charge self-consistent DMFT and the DFT + $U$ calculations, an exchange-correlation functional within the generalized-gradient approximation is used [38].

In DMFT calculations, the Coulomb interaction matrix are parametrized by the Slater integrals with the Coulomb repulsion interaction parameter $U = 6.0$ eV and Hund's exchange interaction parameter $J_{\text{H}} = 1.0$ eV for the calculations in the main text, respectively. The values of $U$ and $J_{\text{H}}$ used in DMFT is determined by matching the computed spectral gap at 290 K to experimentally observed optical band gap at room temperature [31,32]. The self-energy double counting is subtracted via the nominal scheme [40], i.e., $\Sigma_{\text{dc}} = U(n^0_{3d} - 1/2) - J_{\text{H}}/2(n^0_{3d} - 1)$. For $V^{3+}$, we take the nominal occupancy $n^0_{3d} = 2.0$. The hybridization expansion continuous-time quantum impurity solver is employed to solve the Anderson impurity models [41,42].

The $\boldsymbol{k}$ grids of $6 \times 6 \times 2$, $5 \times 3 \times 5$, $6 \times 6 \times 2$, $6 \times 3 \times 3$, and $7 \times 7 \times 1$ are adopted in all self-consistent calculations for bulk $R\bar{3}$, $C2/m$, $P\bar{3}1c$, $C2/c$, and monolayer $VI_3$, respectively. For orbital magnetization calculations denser $\boldsymbol{k}$ grids are employed for the Brillouin-zone samplings ($20 \times 20 \times 1$ for bulk $R\bar{3}$, $P\bar{3}1c$, and monolayer, $16 \times 8 \times 16$ for bulk $C2/m$, $20 \times 10 \times 1$ for bulk $C2/c$).

## III. RESULTS AND DISCUSSION

$VI_3$ has been found to crystallize in different polymorphs owing to different layer stacking with the space groups $R\bar{3}$, $P\bar{3}1c$, $C2/m$, and $C2/c$ [30–33]. The structural phase transitions in $VI_3$, albeit interesting, are very subtle. A summary of experimentally reported crystal structures at low and room temperatures can be found in Appendix A. For simplicity, we will focus exclusively on the $R\bar{3}$ structure for the discussion here for subtle stacking difference is not expected to impact the orbital magnetization in any way significantly. Within each layer, V atoms form a honeycomb lattice, and each V is caged by six $I^-$'s that form edge-sharing octahedra as shown in Fig. 1 (a). In the $R\bar{3}$ structure, a hexagonal primitive cell contains three monolayers, and the vanadium honeycomb lattices display a rhombohedral stacking along crystallographic $c$ direction as shown in Fig. 1(b).

Recent experiments show that the bulk $VI_3$ exhibits an optical band gap of 0.6–0.7 eV [31,32], in contrast to a metallic band structure from a DFT electronic structure calculation as shown in Fig. 5 in Appendix B. By including the static correlation described by Hubbard $U$ (i.e., DFT + $U$), the calculated band structures recover the insulating nature for reasonable $U$ values (see Fig. 5 in Appendix B), indicating that $VI_3$ is indeed Mott insulating. We choose a value of $U_{\text{eff}} = U - J = 4$ eV by matching the computed band gaps (0.67 and 0.64 eV for $R\bar{3}$ and $P\bar{3}1c$, respectively) to experimentally observed optical band gaps at room temperature (0.60 and 0.67 eV for $R\bar{3}$ [31] and $P\bar{3}1c$ [32], respectively). From the projected band structure and density of states for $R\bar{3}$ shown in Figs. 2(a) and 2(b), it can be seen that both $t_{2g}$ and $e_g$ orbitals at V atoms hybridize with $p$ states of iodines. This hybridization is significantly enhanced when compared to the result without $U$ and magnetism as shown in Fig. 2(c). It will shortly be seen that this enhanced mixing may lead to overestimation of the extended contribution to the orbital magnetization.

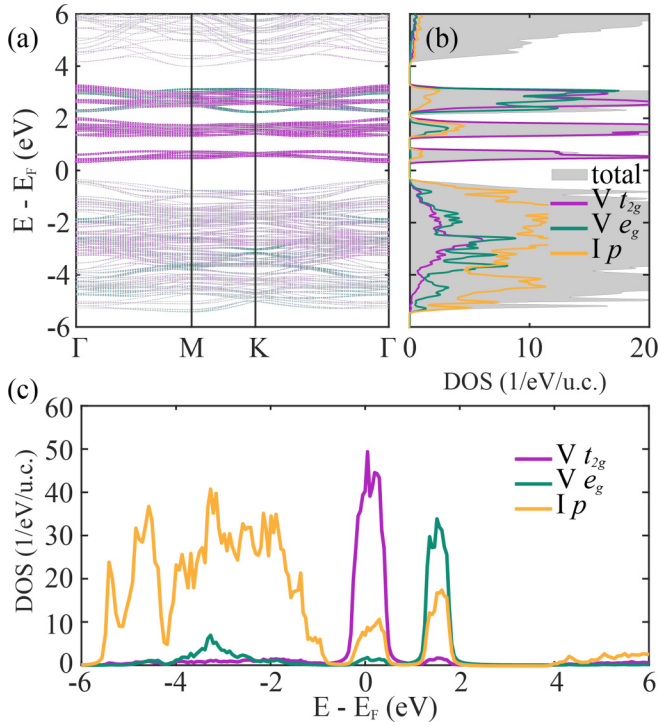


FIG. 2. (a) Projected band structure and (b) density of states of bulk $R\bar{3}$ using DFT + $U$. (c) Projected density of states of bulk $R\bar{3}$ without $U$ and magnetism.

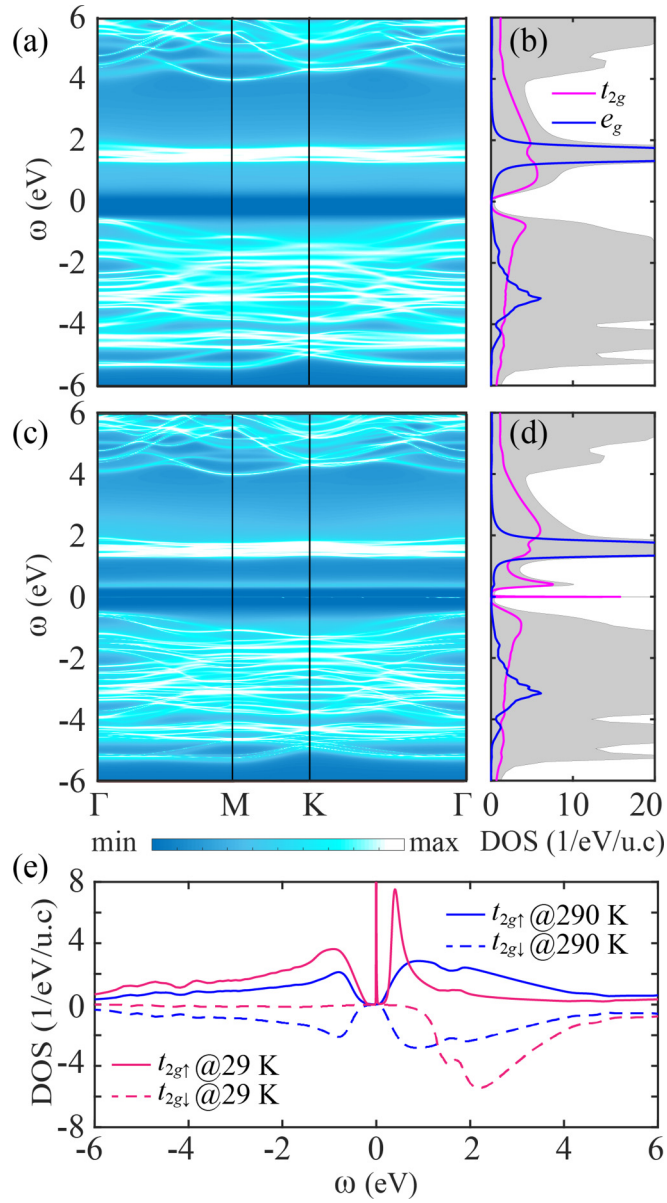


FIG. 3. (a) and (c) are momentum-resolved spectral functions for bulk $VI_3$ in the $R\bar{3}$ space group using the DMFT method at 290 and 29 K, respectively. (b) and (d) are corresponding projected density of states. (e) Spin-resolved density of states.

As DFT + $U$ calculations only capture the static part of electronic correlation, the self-consistent DMFT method is employed to examine the effects of the dynamical correlation [36]. The starting point of a DMFT calculation is a nonmagnetic DFT calculation without $U$, which shows a significant crystal-field splitting between $t_{2g}$ and $e_g$ of 2 eV [see Fig. 2(c)]. Since the crystal-field splitting is larger than the bandwidths of both $t_{2g}$ and $e_g$ sets, Hubbard $U$ is added only to the $t_{2g}$ set in DMFT calculations. We find that inclusion of $e_g$ orbitals into our correlated subspace does not change our main conclusions concerning the orbital magnetizations (see Appendix D). To obtain the spin- and momentum-resolved spectral functions in DMFT calculations, we have performed an analytical continuation of self-energies using the maximum-entropy method [36]. Figures 3(a) and 3(c) are momentum-resolved spectral functions for high-temperature (290 K) paramagnetic and low-temperature (29 K) ferromagnetic phases, respectively. In contrast to the DFT + $U$ result, due to the dramatical renormalization from electronic correlation, the spectral weight of $t_{2g}$ becomes highly smeared out along the energy axis, although the Mott gap is clearly visible in both ferro- and paramagnetic regimes.

Experimentally, $VI_3$ is a ferromagnet with out-of-plane magnetic moments (i.e., along the $z$ direction) and Curie temperature of $T_c \sim 50$ K [30–33]. Our DMFT calculations can reproduce both the low-temperature ferromagnetic and the high-temperature paramagnetic phases. As seen in the spin-resolved density of states shown in Fig. 3(e), the two spin projections of the $t_{2g}$ orbitals are equally populated at 290 K, leading to the paramagnetic phase. At 29 K, the spin-up component dominates, and the system develops a ferromagnetic order. In the low-temperature ferromagnetic phase, there is a quasiparticle peak around the chemical potential as shown in Figs. 3(d) and 3(e). This dynamical singlet, attributable to Kondo resonance, is insensitive to the parameters used in the analytical continuation but is quickly obliterated by thermal fluctuations as the temperature rises. In the ferromagnetic phase, the local spin moment on each V atom obtained from DMFT and DFT + $U$ is 1.88 and 2.00$\mu_B$, respectively, which is close to the expected $S = 1$ state. We will examine next the orbital magnetization at both DFT + $U$ and DMFT levels.

In the DFT + $U$ static mean-field approximation, the orbital magnetizations can be efficiently calculated using the

noninteracting formula in the low-temperature limit,

$$\boldsymbol{M}(\boldsymbol{k}) = -\frac{ie}{2\hbar}\sum_{n} f_{nk}\left\langle \frac{\partial u_{nk}}{\partial \boldsymbol{k}}\right| \times (H_{\boldsymbol{k}} + \varepsilon_{nk} - 2\mu)\left|\frac{\partial u_{nk}}{\partial \boldsymbol{k}}\right\rangle, \quad (1)$$

where $u_{nk}$ is the cell-periodic part of the Bloch function of the $n$th band at crystal momentum $\boldsymbol{k}$, $\varepsilon_{nk}$ is the band dispersion, and $\mu$ is the chemical potential. Brillouin-zone summation of $\boldsymbol{M}(\boldsymbol{k})$ then yields the total orbital magnetic moment. We use the perturbation formula to evaluate $|\partial u_{nk}/\partial \boldsymbol{k}\rangle$,

$$\left|\frac{\partial u_{nk}}{\partial \boldsymbol{k}}\right\rangle = \sum_{m\neq n}\frac{|u_{mk}\rangle\langle u_{mk}|\partial H_{\boldsymbol{k}}/\partial \boldsymbol{k}|u_{nk}\rangle}{\varepsilon_{nk}-\varepsilon_{mk}}. \quad (2)$$

The velocity matrix elements $\langle u_{mk}|\partial H_{\boldsymbol{k}}/\partial \boldsymbol{k}|u_{nk}\rangle$ are obtained using the linear optics module as implemented in the WIEN2K package [34,35,43]. A large number of unoccupied bands (up to ~10 eV above the Fermi level) are included to ensure the convergence of obtained orbital magnetization. The value of the orbital magnetization for the bulk $R\bar{3}$ phase is about $0.02\mu_B$ per V, accounting for about 1% of the spin moment. The orbital magnetic moment of monolayer $VI_3$ is computed to be essentially zero within this approach.

To further incorporate dynamical correlation in the self-consistent DMFT level, the generalized formula for orbital magnetization expressed in terms of interacting Green's functions is used [21]

$$M^{c}(\boldsymbol{k}) = \frac{ie}{2\hbar\beta}\sum_{\omega_n}\epsilon^{abc}\,\mathrm{tr}\left\{\left[H_0 - \mu + \frac{\Sigma}{2}\right]Gv_a(\boldsymbol{k})Gv_b(\boldsymbol{k})G\right\}, \quad (3)$$

where $a$, $b$, and $c$ refer to the Cartesian axes $x, y, z$, $\omega_n = (2n+1)\pi/\beta$, $G(\boldsymbol{k}, i\omega_n)$, and $\Sigma(i\omega_n)$ are Matsubara frequencies, interacting Green's functions, and self-energies, respectively. $v_a(\boldsymbol{k}) = -\partial_{k_a}G^{-1}$ is the velocity operator. In the above formula, a term involving the derivative of self-energy against magnetic-field $B$ has been dropped as the DMFT self-energy cannot depend on $\boldsymbol{B}$ linearly [21]. For $\Sigma = 0$ this formula will reduce to the noninteracting case given in Eq. (1), which can be confirmed by both explicit derivation and numerical calculation. The Matsubara summation is converged with $|n| \leqslant 600$ for 290 K and $|n| \leqslant 2000$ for 29 K.

Remarkably, in the DMFT calculations the computed orbital magnetizations are greatly enhanced compared with the DFT + $U$ results as listed in Table I. The DMFT method gives consistent values of $M^z$ for all bulk structures and a monolayer. This is reasonable in the sense that the local octahedral crystal fields imposed on V atoms are nearly identical in these structures. It should be pointed out that Eq. (3) is derived without considering the entropic contribution and only suitable for low temperatures [14]. Although, the values of $U$ and $J_H$ in our DMFT calculations are chosen by matching the computed spectral gap at 290 K to the experimental optical gap at room temperature [31,32], more calculations show that the calculated orbital magnetizations are similar within a reasonable range of $U$ and $J_H$ values (see Table II in Appendix E).

TABLE I. Calculated orbital magnetization along the $z$ direction for bulk $R\bar{3}$, $P\bar{3}1c$, $C2/m$, $C2/c$, and monolayer $VI_3$ using different methods and temperatures as indicated in each case. Units: $\mu_B$/V.

| | $R\bar{3}$ | $P\bar{3}1c$ | $C2/m$ | $C2/c$ | monolayer |
|---|---|---|---|---|---|
| DFT + $U$ | 0.021 | 0.026 | 0.003 | 0.020 | 0.001 |
| DMFT (290 K) | 0.079 | 0.084 | 0.079 | 0.081 | 0.084 |
| DMFT (29 K) | 0.080 | 0.085 | 0.079 | 0.085 | 0.085 |

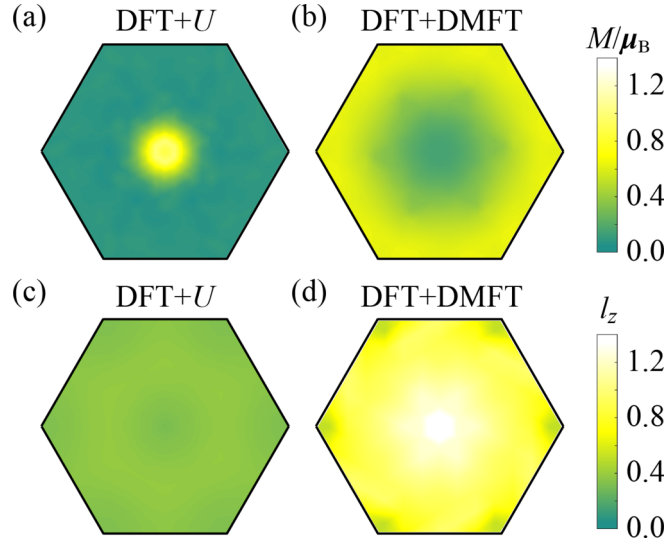


FIG. 4. (a) and (b) are the calculated orbital magnetization distributions in the Brillouin zone (on the $k_z = 0$ plane) for bulk $R\bar{3}$ using DFT + $U$ and DMFT (29 K), respectively. (c) and (d) are the calculated orbital angular momentum distributions in the Brillouin zone (at the $k_z = 0$ plane) for bulk $R\bar{3}$ using DFT + $U$ and DMFT (29 K), respectively.

In order to further analyze how the dynamical correlation influences orbital magnetization, we plot the orbital magnetization $M^z(\boldsymbol{k})$ across the Brillouin zone from both DFT + $U$ and DMFT calculations for the $R\bar{3}$ structure as shown in Figs. 4(a) and 4(b). It is obvious that the distributions of orbital magnetization in the Brillouin zone are quite different for these two methods. In the DFT + $U$ method, the main contribution to orbital magnetization comes from the Brillouin zone center, whereas the orbital magnetization accumulates mainly along the Brillouin-zone boundaries for the DMFT result. The distribution of $M^z(\boldsymbol{k})$ from DFT + $U$ is more localized compared to the DMFT result, which means the orbital magnetization in real space should be more extended in the DFT + $U$ result. This difference can be partially attributed to the enhanced $d$-$p$ mixing in the DFT + $U$ electronic structures as mentioned earlier. Another source of the difference is the dramatical renormalization of the electronic structures through the DMFT self-energy as shown in the spectral functions above [Figs. 3(a) and 3(c)]. The overall effects lead to an over fourfold enhancement of total orbital magnetization compared to the DFT + $U$ result. It is noteworthy that the orbital magnetization is along the $z$ direction, thus, it will lead to strong anisotropy of saturation magnetization, which is consistent with the experimental observation [30–32].

Since in the atomic limit, the orbital magnetization originates from orbital angular momentum, we have performed a further analysis to elucidate the correlation effect on the orbital angular momentum of Bloch wave functions. As the

net residual orbital angular momentum can come from the imbalanced occupation of $d$ orbitals of vanadium atoms, we have projected the Bloch wave functions to the five channels of the spherical harmonics $Y_2^m$ with $m = 0, \pm 1, \pm 2$. The $\boldsymbol{k}$-resolved orbital angular momentum is defined as

$$l_z(\boldsymbol{k}) = \sum_{n\in \mathrm{occ}} \sum_m m \left| \langle \psi_{n\boldsymbol{k}} | Y_2^m \rangle \right|^2, \tag{4}$$

where the summation is over the occupied states. $\psi_{n\boldsymbol{k}}$ is the Bloch wave functions. The results for the bulk $R\bar{3}$ structure are shown in Figs. 4(c) and 4(d). It can be seen that for both the methods, distributions of the orbital angular momentum in $\boldsymbol{k}$ space are almost uniform, especially for the DFT + $U$ method. The reason behind such a behavior can be understood in terms of strong localization of $d$ orbitals on V atoms, leading to weak $\boldsymbol{k}$ dependence of the orbital angular momentum. However, the values of the orbital angular momentum from DMFT is greatly enhanced compared to that from DFT + $U$. The integrated $l_z$ for DFT + $U$ and DMFT are 0.060 and 0.158/V, respectively. Note that for an atomic model with two electrons filling the $t_{2g}$ orbitals of V atoms, according to Hund's rules, the orbital magnetic moment should be 1 $\mu_B$/V and antiparallel to the 2 $\mu_B$/V spin moment [44]. However, the experimental observations show that the out-of-plane magnetic moments are larger than the in-plane ones [30–32], indicating that the orbital magnetic moment should be parallel to the spin moment. In our DMFT paper, we find the orbital moments of ~0.08 $\mu_B$/V parallel to spin moments, consistent with the experimental observations. Our results imply that the orbital magnetization in real materials cannot be simply explained by the atomic model.

Hence, a unified physical picture for dynamically enhanced orbital magnetization in $VI_3$ emerges from the above comparison. Despite a stronger $p$-$d$ mixing in DFT + $U$ that increases the intercellular electronic circulations of electrons [corresponding to the hot spot in Fig. 4(a)], it suppresses the (potentially more important) intracellular circulations at the same time. The overall effect is minimal occupational imbalance among $l_z$ channels and quenched orbital angular momentum. In the self-consistent DMFT framework, the localization behavior of correlated electrons in $VI_3$ is found to increase the occupational imbalance of $l_z$ channels dramatically. Although the orbital hybridizations in crystals will still suppress the orbital magnetization, the greatly enhanced residual orbital angular momentum eventually leads to a significantly enhanced orbital magnetization in the DMFT approach when compared to that from DFT + $U$.

Further insights can be obtained by separating the orbital magnetization into local ($\boldsymbol{M}_{\mathrm{LC}}$) and itinerant ($\boldsymbol{M}_{\mathrm{IC}}$) parts, leading support to the foregoing picture. As defined by Thonhauser *et al.* [12],

$\boldsymbol{M}_{\mathrm{LC}} = -ie/(2N\hbar) \sum_{n\boldsymbol{k}} f_{n\boldsymbol{k}} \langle \nabla_{\boldsymbol{k}} u_{n\boldsymbol{k}}| \times H_{\boldsymbol{k}} |\nabla_{\boldsymbol{k}} u_{n\boldsymbol{k}}\rangle$ and

$\boldsymbol{M}_{\mathrm{IC}} = -ie/(2N\hbar) \sum_{n\boldsymbol{k}} f_{n\boldsymbol{k}} \langle \nabla_{\boldsymbol{k}} u_{n\boldsymbol{k}}| \times |\nabla_{\boldsymbol{k}} u_{n\boldsymbol{k}}\rangle \varepsilon_{n\boldsymbol{k}}$. For DFT + $U$ case, these two parts can be calculated according to the above formulas separately. In order to compare the results given by DFT + $U$ and DMFT on equal footing, we need some approximations for the DMFT case. Specifically, we used the eigenenergies from the DFT step but corrected by the real part of self-energy at the infinity frequency, corresponding to a shift of chemical potential to ensure a proper electron number, i.e., $\varepsilon_{n\boldsymbol{k}}^{\mathrm{DMFT}} \approx \varepsilon_{n\boldsymbol{k}}^{\mathrm{DFT}} + \mathrm{Re}\,\Sigma_\infty$. As the $d$-$p$ mixing is directly related to the itinerant motion of electrons, it is indeed found that in the DFT + $U$ results, the itinerant contribution dominates the orbital magnetization ($M_{\mathrm{LC}}^z = -0.012\mu_B$/V and $M_{\mathrm{IC}}^z = 0.033\mu_B$/V). However, the orbital magnetization is dominated by the local part in the DMFT framework ($M_{\mathrm{LC}}^z = 0.208\mu_B$/V and $M_{\mathrm{IC}}^z = -0.148\mu_B$/V) due to the localization behavior of V atoms.

## IV. CONCLUSION

To summarize, we have studied the electronic correlation effect on orbital magnetization, taking the layered van der Waals magnetic materials $VI_3$ as an example. Our calculations reveal that the dynamical correlation is crucial for evaluating the orbital magnetization in correlated materials, such as $VI_3$. The static mean-field theory based density-functional theory (in the DFT + $U$ level) is insufficient to capture the renormalization to spectral functions and the localization behavior of correlated electrons. As a result, it will underestimate the intracellular circulations contribution to orbital magnetization for these materials. Making use of the state-of-the-art dynamical mean-field theory, we are able to recover the dynamical correlation and give a better description to orbital magnetization, which is consistent with the experimental observation [30–32]. It is interesting that the correlation effect can stabilize the orbital magnetization in the monolayer limit, which clearly warrants future experimental studies with a particular interest in low-dimensional magnetism as well as potential spintronics applications. Theoretically, the effects of nonlocal correlations on the orbital magnetization will be an interesting direction to pursue in the immediate future, which may require cluster- or GW-DMFT methods [45–47].

## ACKNOWLEDGMENTS

This work was supported by the National Natural Science Foundation of China (Grants No. 11725415 and No. 11934001), the Ministry of Science and Technology of China (Grants No. 2018YFA0305601 and No. 2016YFA0301004), and by the Strategic Priority Research Program of Chinese Academy of Science (Grant No. XDB28000000).

## APPENDIX A: REVIEW OF THE SUBTLE STRUCTURAL PHASE TRANSITIONS IN $VI_3$

The structural phase transitions in $VI_3$ is very subtle and still under debate. Tian *et al.* [30] claim that the structural phase transition of $VI_3$ is analogous to the structural transition of $CrI_3$, i.e., between the high-temperature monoclinic structure $C2/m$ and the low-temperature rhombohedral structure $R\bar{3}$ with $T_s = 79$ K. Son *et al.* [32] report that $VI_3$ is in the space-group $P\bar{3}1c$ under room temperature with a structural phase transition to monoclinic $C2/c$ at $T_s = 79$ K. Kong *et al.* [31] have determined the $R\bar{3}$ structure at 100 K and suggest a subtle structural phase transition at 78 K. Doležal *et al.* [48] also observe a structural phase transition from

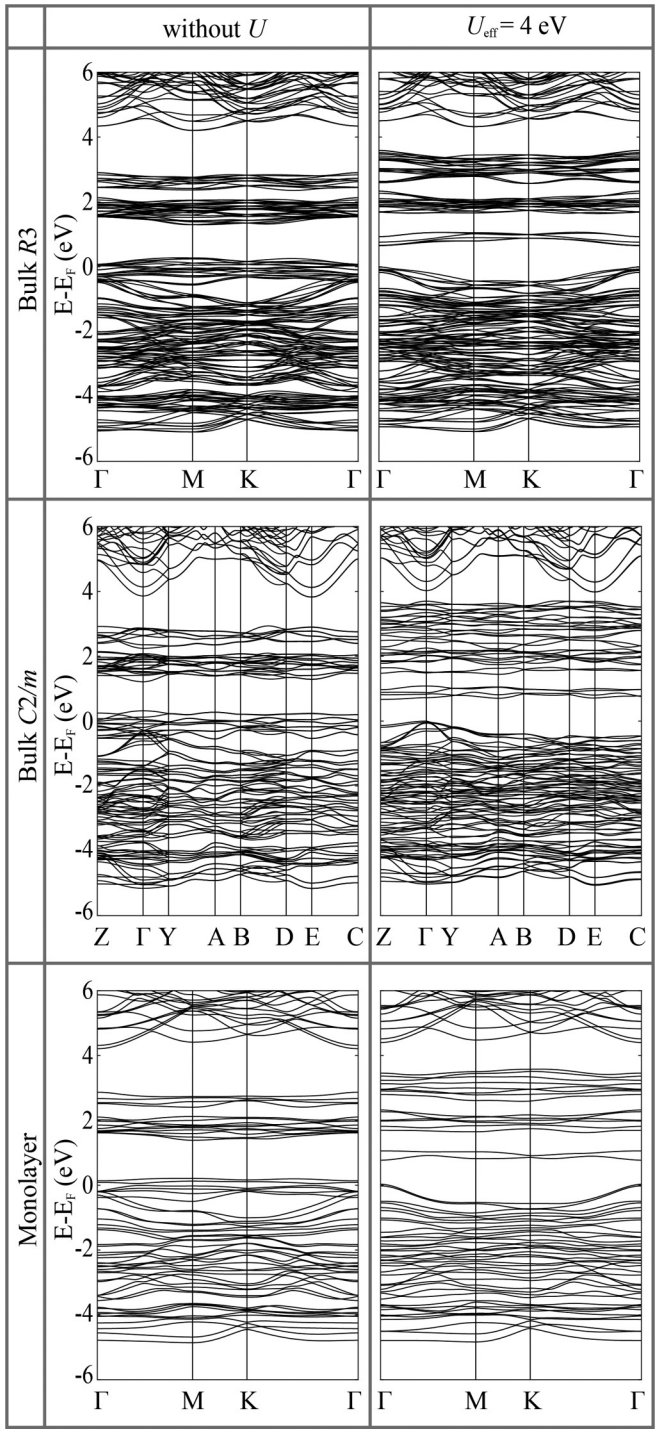


FIG. 5. Band structures of bulk $R\bar{3}$, $C2/m$, and monolayer $VI_3$ with and without $U$.

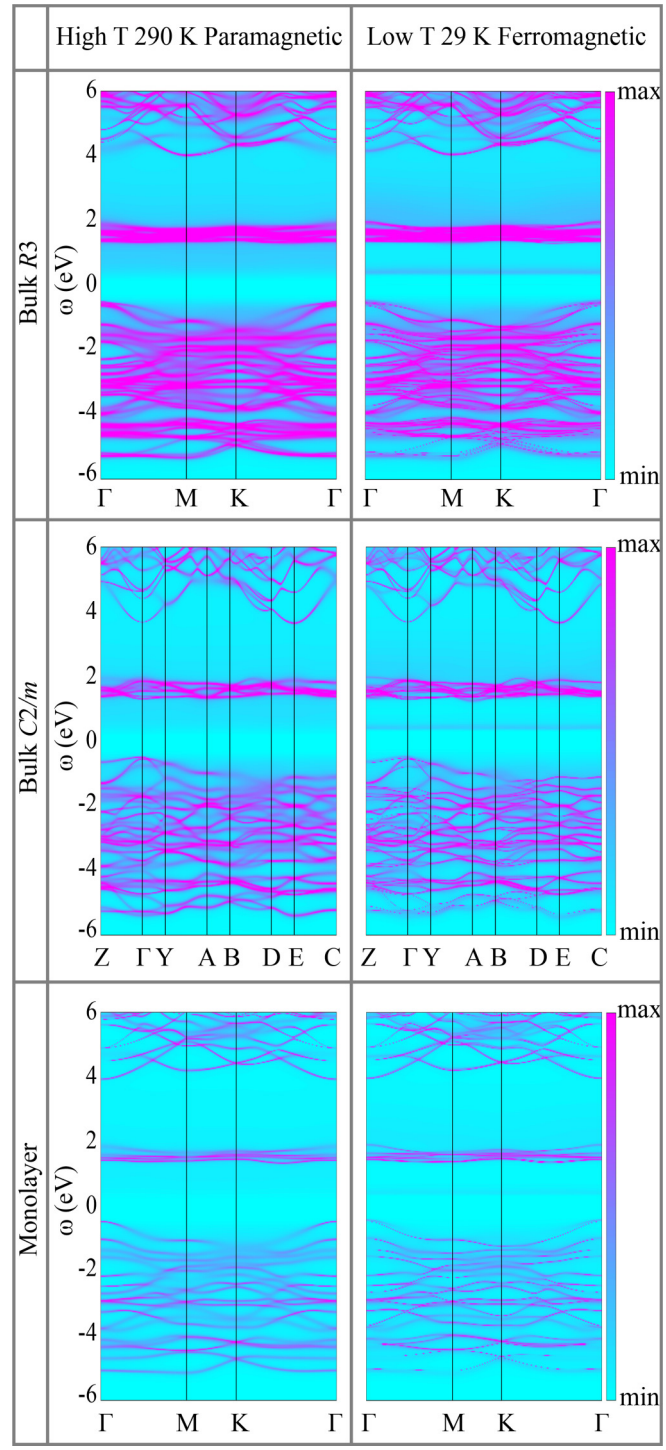


FIG. 6. DMFT spectral functions for bulk $R\bar{3}$, $C2/m$, and monolayer $VI_3$ under low (29 K) and high (290 K) temperatures. $U = 6.0$, $J_H = 1.0$ eV.

high-temperature $R\bar{3}$ to low-temperature monoclinic structure. Although the structural phase transitions are very interesting, they are complicated and not the aim of this paper. The subtle stacking differences of these possible structures are not expected to impact the orbital magnetization in any way significant. We then calculated the orbital magnetizations for these possible structures but only focus on the $R\bar{3}$ structure for discussions in the main text for simplicity. We also show in our calculations that the main conclusions concerning orbital magnetization drawn for the $R\bar{3}$ structure remain unaltered for all crystal structures of $VI_3$.

## APPENDIX B: DFT and DFT + $U$ BAND STRUCTURES

Here we show the calculated band structures of bulk $R\bar{3}$, $C2/m$, and monolayer $VI_3$ with and without $U$ (see

Fig. 5). The results for $P\bar{3}1c$ and $C2/c$ are similar to them. For brevity, they are not shown here. We can see that without the Hubbard $U$ correction, they are all metallic. By including the Hubbard $U$ correction ($U_{\text{eff}} = U - J = 4$ eV), the calculated band structures recover the insulating nature, indicating that $VI_3$ is indeed Mott insulating.

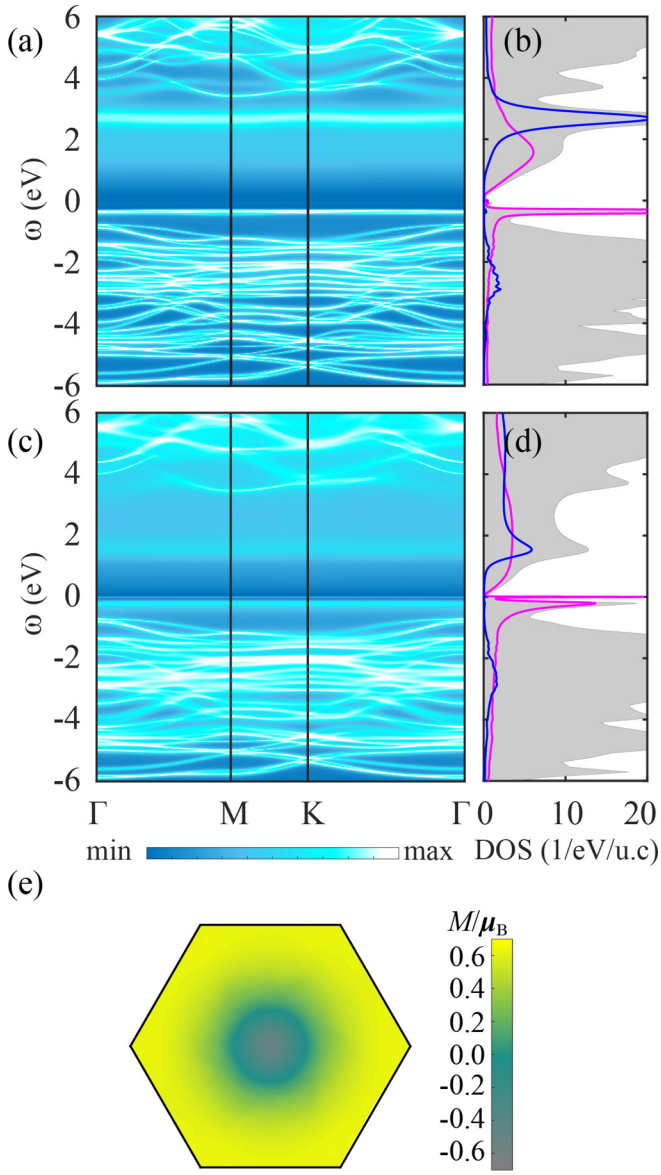


FIG. 7. (a) and (c) are momentum-resolved spectral functions for bulk $VI_3$ in the $R\bar{3}$ space group using the DMFT method under 290 and 29 K, respectively. (b) and (d) are corresponding projected density of states. In contrast to the results in main text, here all $t_{2g}$ and $e_g$ orbitals of V are treated as correlated orbitals. (e) Calculated orbital magnetization distribution in the Brillouin zone (at the $k_z = 0$ plane) for bulk $VI_3$ using DMFT (29 K).

## APPENDIX C: DMFT SPECTRAL FUNCTIONS

Here we show the calculated DMFT spectral functions of bulk $R\bar{3}$, $C2/m$, and monolayer $VI_3$ at high (290 K) and low (29 K) temperatures (see Fig. 6). The results for $P\bar{3}1c$ and $C2/c$ are similar to them. For brevity, they are not shown here. We can see that they are all Mott insulating at both low and high temperatures.

## APPENDIX D: VALIDATION OF THE CHOICE OF CORRELATED SUBSPACE

In order to examine the reliability of the approximation that only $t_{2g}$ set is treated as correlated, we have performed further calculations to treat all $t_{2g}$ and $e_g$ states as the correlated manifold. Note that after taking into account the $e_g$ states, the screening from the uncorrelated shells decreased. Thus, we need a larger Coulomb $U$ to obtain a similar spectral gap. Here, we have chosen $U = 10$ eV. The results are shown in Fig. 7. We can see that the resulted spectral functions are similar except that the energy dispersion of $t_{2g}$ orbitals below the Fermi level becomes narrower, leading to a reduced $p$-$d$ hybridization. The obtained orbital magnetization for bulk $VI_3$ (space-group $R\bar{3}$) at 29 K is only slightly reduced from 0.080

TABLE II. Calculated orbital magnetization along the $z$ direction for bulk $R\bar{3}$, $C2/m$, and monolayer $VI_3$ using DFT + DMFT with different $U$ and $J_H$ parameters under low (29 K) and high (290 K) temperatures.

| Structure | $U$ (eV) | $J_H$ (eV) | $T$ (K) | $M_{\text{orb}}$ ($\mu_B$/V) |
|---|---|---|---|---|
| $R\bar{3}$ | 5.0 | 0.8 | 29 | 0.079 |
| | | | 290 | 0.078 |
| | | 1.0 | 29 | 0.084 |
| | | | 290 | 0.070 |
| | 6.0 | 0.8 | 29 | 0.078 |
| | | | 290 | 0.078 |
| | | 1.0 | 29 | 0.080 |
| | | | 290 | 0.079 |
| $C2/m$ | 5.0 | 0.8 | 29 | 0.078 |
| | | | 290 | 0.077 |
| | | 1.0 | 29 | 0.085 |
| | | | 290 | 0.079 |
| | 6.0 | 0.8 | 29 | 0.077 |
| | | | 290 | 0.078 |
| | | 1.0 | 29 | 0.079 |
| | | | 290 | 0.079 |
| Monolayer | 5.0 | 0.8 | 29 | 0.084 |
| | | | 290 | 0.082 |
| | | 1.0 | 29 | 0.089 |
| | | | 290 | 0.084 |
| | 6.0 | 0.8 | 29 | 0.084 |
| | | | 290 | 0.083 |
| | | 1.0 | 29 | 0.085 |
| | | | 290 | 0.084 |

to $0.073\mu_B$/V, which can be attributed to the reduced *p-d* mixing. Although including both the $t_{2g}$ and the $e_g$ sets in the correlated subspace leads to a correction to the final orbital magnetization, our conclusions remain valid. In this sense, the approximation to only treat the $t_{2g}$ manifold as our correlated subspace is reasonable.

## APPENDIX E: THE DEPENDENCY OF $M$ ON $U$ AND $J_H$

More calculations show that the calculated orbital magnetizations are similar within a reasonable range of $U$ and $J_H$ values (see Table II).


[1] J. W. Taylor, J. A. Duffy, A. M. Bebb, M. R. Lees, L. Bouchenoire, S. D. Brown, and M. J. Cooper, Phys. Rev. B **66**, 161319(R) (2002).

[2] H. J. Gotsis and I. I. Mazin, Phys. Rev. B **68**, 224427 (2003).

[3] S. Qiao, A. Kimura, H. Adachi, K. Iori, K. Miyamoto, T. Xie, H. Namatame, M. Taniguchi, A. Tanaka, T. Muro, S. Imada, and S. Suga, Phys. Rev. B **70**, 134418 (2004).

[4] M. A. Laguna-Marco, D. Haskel, N. Souza-Neto, J. C. Lang, V. V. Krishnamurthy, S. Chikara, G. Cao, and M. van Veenendaal, Phys. Rev. Lett. **105**, 216407 (2010).

[5] A. Kolchinskaya, P. Komissinskiy, M. B. Yazdi, M. Vafaee, D. Mikhailova, N. Narayanan, H. Ehrenberg, F. Wilhelm, A. Rogalev, and L. Alff, Phys. Rev. B **85**, 224422 (2012).

[6] S. Murakami, Phys. Rev. Lett. **97**, 236805 (2006).

[7] D. Xiao, Y. Yao, Z. Fang, and Q. Niu, Phys. Rev. Lett. **97**, 026603 (2006).

[8] D. Xiao, W. Yao, and Q. Niu, Phys. Rev. Lett. **99**, 236809 (2007).

[9] Z. Wang and P. Zhang, Phys. Rev. B **76**, 064406 (2007).

[10] A. M. Essin, A. M. Turner, J. E. Moore, and D. Vanderbilt, Phys. Rev. B **81**, 205104 (2010).

[11] D. Xiao, J. Shi, and Q. Niu, Phys. Rev. Lett. **95**, 137204 (2005).

[12] T. Thonhauser, D. Ceresoli, D. Vanderbilt, and R. Resta, Phys. Rev. Lett. **95**, 137205 (2005).

[13] D. Ceresoli, T. Thonhauser, D. Vanderbilt, and R. Resta, Phys. Rev. B **74**, 024408 (2006).

[14] J. Shi, G. Vignale, D. Xiao, and Q. Niu, Phys. Rev. Lett. **99**, 197202 (2007).

[15] K.-T. Chen and P. A. Lee, Phys. Rev. B **84**, 205137 (2011).

[16] R. Bianco and R. Resta, Phys. Rev. Lett. **110**, 087202 (2013).

[17] S. A. Nikolaev and I. V. Solovyev, Phys. Rev. B **89**, 064428 (2014).

[18] T. Woźniak, P. E. Faria Junior, G. Seifert, A. Chaves, and J. Kunstmann, Phys. Rev. B **101**, 235408 (2020).

[19] F. Xuan and S. Y. Quek, Phys. Rev. Res. **2**, 033256 (2020).

[20] T. Deilmann, P. Krüger, and M. Rohlfing, Phys. Rev. Lett. **124**, 226402 (2020).

[21] R. Nourafkan, G. Kotliar, and A. M. S. Tremblay, Phys. Rev. B **90**, 125132 (2014).

[22] F. Aryasetiawan, K. Karlsson, and T. Miyake, Phys. Rev. B **93**, 161104(R) (2016).

[23] T. J. Sjöstrand, K. Karlsson, and F. Aryasetiawan, Phys. Rev. B **100**, 054427 (2019).

[24] S. Acheche, R. Nourafkan, and A. M. S. Tremblay, Phys. Rev. B **99**, 075144 (2019).

[25] N. D. Mermin and H. Wagner, Phys. Rev. Lett. **17**, 1133 (1966).

[26] P. Ajayan, P. Kim, and K. Banerjee, Phys. Today **69**(9), 38 (2016).

[27] Z. Wang, T. Zhang, M. Ding, B. Dong, Y. Li, M. Chen, X. Li, J. Huang, H. Wang, X. Zhao, Y. Li, D. Li, C. Jia, L. Sun, H. Guo, Y. Ye, D. Sun, Y. Chen, T. Yang, J. Zhang, S. Ono, Z. Han, and Z. Zhang, Nat. Nanotechnol. **13**, 554 (2018).

[28] T. Song, X. Cai, M. W. Y. Tu, X. Zhang, B. Huang, N. P. Wilson, K. L. Seyler, L. Zhu, T. Taniguchi, K. Watanabe, M. A. McGuire, D. H. Cobden, D. Xiao, W. Yao, and X. Xu, Science **360**, 1214 (2018).

[29] D. R. Klein, D. MacNeill, J. L. Lado, D. Soriano, E. Navarro-Moratalla, K. Watanabe, T. Taniguchi, S. Manni, P. Canfield, J. Fernández-Rossier, and P. Jarillo-Herrero, Science **360**, 1218 (2018).

[30] S. Tian, J.-F. Zhang, C. Li, T. Ying, S. Li, X. Zhang, K. Liu, and H. Lei, J. Am. Chem. Soc. **141**, 5326 (2019).

[31] T. Kong, K. Stolze, E. I. Timmons, J. Tao, D. Ni, S. Guo, Z. Yang, R. Prozorov, and R. J. Cava, Adv. Mater. **31**, 1808074 (2019).

[32] S. Son, M. J. Coak, N. Lee, J. Kim, T. Y. Kim, H. Hamidov, H. Cho, C. Liu, D. M. Jarvis, P. A. C. Brown, J. H. Kim, C.-H. Park, D. I. Khomskii, S. S. Saxena, and J.-G. Park, Phys. Rev. B **99**, 041402(R) (2019).

[33] E. Gati, Y. Inagaki, T. Kong, R. J. Cava, Y. Furukawa, P. C. Canfield, and S. L. Budâko, Phys. Rev. B **100**, 094408 (2019).

[34] P. Blaha, K. Schwarz, G. K. H. Madsen, D. Kvasnicka, J. Luitz, R. Laskowski, F. Tran, and L. D. Marks, WIEN2K, *An Augmented Plane Wave + Local Orbitals Program for Calculating Crystal Properties* (Karlheinz Schwarz, Techn. Universität Wien, Austria, 2018).

[35] P. Blaha, K. Schwarz, F. Tran, R. Laskowski, G. K. H. Madsen, and L. D. Marks, J. Chem. Phys. **152**, 074101 (2020)

[36] K. Haule, C.-H. Yee, and K. Kim, Phys. Rev. B **81**, 195107 (2010).

[37] G. Kresse and J. Furthmüller, Phys. Rev. B **54**, 11169 (1996).

[38] J. P. Perdew, K. Burke, and M. Ernzerhof, Phys. Rev. Lett. **77**, 3865 (1996).

[39] V. I. Anisimov, I. V. Solovyev, M. A. Korotin, M. T. Czyżyk, and G. A. Sawatzky, Phys. Rev. B **48**, 16929 (1993).

[40] L. V. Pourovskii, B. Amadon, S. Biermann, and A. Georges, Phys. Rev. B **76**, 235101 (2007).

[41] P. Werner, A. Comanac, L. de' Medici, M. Troyer, and A. J. Millis, Phys. Rev. Lett. **97**, 076405 (2006).

[42] K. Haule, Phys. Rev. B **75**, 155113 (2007).

[43] C. Ambrosch-Draxl and J. O. Sofo, Comput. Phys. Commun. **175**, 1 (2006).

[44] G. L. Stamokostas and G. A. Fiete, Phys. Rev. B **97**, 085150 (2018).

[45] M. H. Hettler, A. N. Tahvildar-Zadeh, M. Jarrell, T. Pruschke, and H. R. Krishnamurthy, Phys. Rev. B **58**, R7475(R) (1998).
[46] G. Kotliar, S. Y. Savrasov, G. Pálsson, and G. Biroli, Phys. Rev. Lett. **87**, 186401 (2001).
[47] F. Nilsson and F. Aryasetiawan, Computation **6**, 26 (2018).
[48] P. Doležal, M. Kratochvílová, V. Holý, P. Čermák, V. Sechovský, M. Dušek, M. Míšek, T. Chakraborty, Y. Noda, S. Son, and Je-Geun Park, Phys. Rev. Mater. **3**, 121401(R) (2019).